Journal of Advanced Ceramics
2022, **11**(8): 1307–1318
https://doi.org/10.1007/s40145-022-0612-4

ISSN 2226-4108
CN 10-1154/TQ

Research Article

Maximizing the mechanical performance of Ti_3AlC_2-based MAX phases with aid of machine learning

Xingjun DUAN[a,†], Zhi FANG[a,†], Tao YANG[a], Chunyu GUO[a], Zhongkang HAN[b], Debalaya SARKER[c], Xinmei HOU[a,*], Enhui WANG[a,*]

[a]*Beijing Advanced Innovation Center for Materials Genome Engineering*, *Collaborative Innovation Center of Steel Technology*, *University of Science and Technology Beijing*, *Beijing 100083*, *China*
[b]*Fritz-Haber-Institut der Max-Planck-Gesellschaft*, *Faradayweg 4-6*, *Berlin 14195*, *Germany*
[c]*UGC-DAE Consortium for Scientific Research*, *University Campus*, *Khandwa Road*, *Indore 452001*, *India*

Received: March 5, 2022; Revised: May 1, 2022; Accepted: May 13, 2022

Abstract: Mechanical properties consisting of the bulk modulus, shear modulus, Young's modulus, Poisson's ratio, etc., are key factors in determining the practical applications of MAX phases. These mechanical properties are mainly dependent on the strength of M–X and M–A bonds. In this study, a novel strategy based on the crystal graph convolution neural network (CGCNN) model has been successfully employed to tune these mechanical properties of Ti_3AlC_2-based MAX phases via the A-site substitution ($Ti_3(Al_{1-x}A_x)C_2$). The structure–property correlation between the A-site substitution and mechanical properties of $Ti_3(Al_{1-x}A_x)C_2$ is established. The results show that the thermodynamic stability of $Ti_3(Al_{1-x}A_x)C_2$ is enhanced with substitutions A = Ga, Si, Sn, Ge, Te, As, or Sb. The stiffness of Ti_3AlC_2 increases with the substitution concentration of Si or As increasing, and the higher thermal shock resistance is closely associated with the substitution of Sn or Te. In addition, the plasticity of Ti_3AlC_2 can be greatly improved when As, Sn, or Ge is used as a substitution. The findings and understandings demonstrated herein can provide universal guidance for the individual synthesis of high-performance MAX phases for various applications.

Keywords: $Ti_3(Al_{1-x}A_x)C_2$; crystal graph convolution neural network (CGCNN) model; stability; mechanical properties

1 Introduction

$M_{n+1}AX_n$ phases are a kind of ternary layered materials belonging to a hexagonal crystal system, where M is the early transition metal, A represents the group 13–16 element, X denotes C or N, and n is the integer [1]. The specific layered structure and chemical bond characteristics endow MAX phases with extraordinary ceramic properties (good mechanical properties, high oxidation, corrosion resistance, etc.) and metallic properties (excellent machinability, high thermal shock resistance, etc.). These merits allow the MAX phases to become promising candidates for aerospace, metallurgy, chemical engineering, and so forth [2–5]. Practical applications of the MAX phases are largely determined by their mechanical properties consisting

† Xingjun Duan and Zhi Fang contributed equally to this work.

* Corresponding authors.
E-mail: X. Hou, houxinmeiustb@ustb.edu.cn;
E. Wang, wangenhui@ustb.edu.cn

of the elastic modulus, Poisson's and Pugh's ratios, etc. [6]. Benefited from the intrinsic ceramic and metallic features, the MAX phases exhibit diverse mechanical properties over a wide range [7,8]. On one hand, the MAX phases with a high elastic modulus possess higher strength and thus can be used as structural materials [8,9]. However, due to the weak M–A metallic bonds, the Vickers hardness (around 2–8 GPa) of MAX phases is much smaller than those of traditional ceramic materials (e.g., Si_3N_4 (19–69 GPa), AlON (16.7 GPa), and Al_2O_3/SiO_2 (18 GPa)) [10–13], which leads to poor long-term stability. On the other hand, the MAX phases with a low elastic modulus possess better ductility, plasticity, and thermal shock resistance, exhibiting a huge potential in barrier coatings [14,15]. Nonetheless, the strong M–X covalent bonds prevent the reduction of elastic modulus, which tends to result in the failure of barrier coatings. Therefore, the extension of upper and lower limits on mechanical properties for the MAX phases has become an urgent task for their engineering application.

The strengths of M–X and M–A bonds are key factors in controlling the ceramic or metallic properties of MAX phases, hinting that tailoring the constituent elements for M, A, or X sites by the solid solution method should be an effective approach to tune the mechanical properties [16–19]. Gao *et al.* [20] have reported that the Si substitution at the A-site could increase the elastic modulus of $Ti_3(Al_{1-x}Si_x)C_2$ solid solution, thus leading to higher Vickers hardness contributed by the stronger M–A bonds. Dubois *et al.* [21] have found that higher Sn concentration at the A-site reduced the elastic modulus of $Ti_3(Sn_{1-x}Al_x)C_2$ solid solution, which is caused by the weakening effect of Ti–Sn bonds. Therefore, the optimizations of the elastic moduli of MAX phases should focus on the adjustment of the M–A bond strength via tuning the A-site chemical composition. However, most existing experiments rely on the trial–error method, and the amount of data obtained remains limited, resulting in a lack of the structure–property relationship of MAX phases. Therefore, it is unfavorable for guiding the screening of the upper and lower limit of mechanical properties of new MAX phases. Besides experimental studies, the commonly used high-throughput computing within the framework of density functional theory (DFT) can scan over a large number of samples for the rational design of desired properties [22,23]. However, the one-by-one scanning with DFT requires a large investment of time and effort when dealing with complex material systems. This imposes a limitation on the rapid search and precise design of new materials [24,25]. Therefore, a more effective method of predicting new MAX phases with tunable mechanical properties is urgently required.

Recently, with the availability of large material databases, data-driven machine learning (ML) methods for material design and discovery have gained much attention due to their potential to predict new materials with desirable properties more quickly and precisely [36–29]. Among all ML methods, the majority employ the features and properties of the samples to train data and are not fully capable of providing the needed structure–property correlations for the MAX phases. Fortunately, the crystal graph convolution neural network (CGCNN) model [30], which utilizes the crystallographic information file (CIF), can establish a relationship between different crystal structures and materials' physical properties. This method can efficiently predict the properties of crystal structures of new MAX phases. Nevertheless, the CIFs as inputs without optimized structures always reduce the accuracy of prediction results. Therefore, a necessary correction is required for further improving the CGCNN model.

In this work, Ti_3AlC_2, a typical representative of MAX phases, has been adopted to build a series of $Ti_3(Al_{1-x}A_x)C_2$ (x = 0, 0.125, 0.25, 0.375, 0.5, 0.625, 0.75, 0.875, and 1) via the A-site substitution. The relationship between the crystal structures and mechanical properties is then established via the CGCNN model, so as to design the potential MAX phases possessing better and tunable mechanical properties. In addition, a linear correction method for inputting CIFs is proposed, aiming to increase the accuracy of prediction results as per the level of DFT calculations. Based on this, the effects of different substitution elements on the strengths of M–X and M–A bonds together with the upper and lower limits of mechanical properties in MAX phases are elucidated.

2 Methods

In this work, nineteen elements that may occupy the A-site of the MAX phases have been selected as substitutions for $Ti_3(Al_{1-x}A_x)C_2$ (A = Si, P, S, Cu, Zn, Ga, Ge, As, Se, Cd, In, Sn, Sb, Te, Au, Hg, Tl, Pb, or Bi) to tune their mechanical properties rationally and efficiently. The strategy is shown in Fig. 1. For the

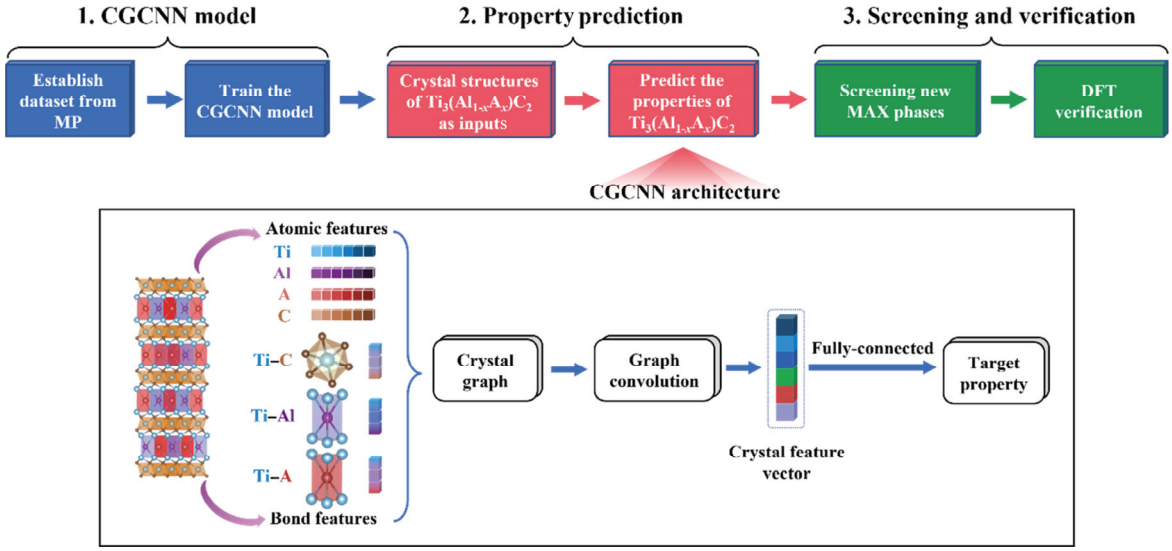

Fig. 1 Schematic diagram of screening new MAX phases with tunable mechanical properties based on CGCNN model.

CGCNN model, it is difficult to capture the minute changes in the crystal structures of $Ti_3(Al_{1-x}A_x)C_2$ caused by the A-site substitution, resulting in unsatisfactory prediction accuracy. To solve this issue, the design strategy of $Ti_3(Al_{1-x}A_x)C_2$ is proposed as follows. Firstly, datasets are created with the data obtained from the Materials Project (MP) [31]. The CGCNN model optimized via the activation function and hyperparameters is trained to establish a relationship between crystal structures and properties. Secondly, the crystal structures of $Ti_3(Al_{1-x}A_x)C_2$ optimized via the linear correction method are used as the inputs, followed by the prediction of the stability and mechanical properties through the trained model. Finally, the stable $Ti_3(Al_{1-x}A_x)C_2$ with tunable mechanical properties have been selected for the DFT calculations to verify the validity of optimized CGCNN model.

2. 1 CGCNN model

The CGCNN model used in this work utilizes an undirected multigraph-crystal graph consisting of the atom feature vector v_i and the bond feature vector $u_{(i,j)_k}$ to represent the crystal structures of $Ti_3(Al_{1-x}A_x)C_2$, as shown in Fig. 1. The atom feature vectors have been iteratively updated by the convolution function expressed as Eq. (1):

$$v_i^{(t+1)} = v_i^{(t)} + \sum_{j,k} \sigma(z_{(i,j)_k}^{(t)} W_c^{(t)} + b_c^{(t)}) \odot g(z_{(i,j)_k}^{(t)} W_s^{(t)} + b_s^{(t)}) \quad (1)$$

where $z_{(i,j)_k}^{(t)} = v_i^{(t)} \oplus v_j^{(t)} \oplus u_{(i,j)_k}^{(t)}$ is the concatenated vector formed via connecting all the atom and bond feature vectors, $\odot$ denotes the matrix elementwise multiplication, $W_c^{(t)}$, $W_s^{(t)}$, and $b^{(t)}$ are the convolution weight matrix, the self-weight matrix, and the bias of the t-th layer, respectively, and σ and g represent the sigmoid function and the nonlinear activation function, respectively. Herein, the hyperbolic tangent function is applied to replace the softplus function used in the original CGCNN model, because it can regularize the latent vector. This regularization is able to assemble the eigenvectors of crystals with similar properties, which can improve the accuracy and interpretability of the model [32].

The implementation of CGCNN model is based on the Pytorch. The same initial atomic feature vectors as the original CGCNN model are used [30]. In addition, a neural network consisting of five convolutional layers and two fully connected hidden layers is utilized to train models and predict properties. The crystal structures and property parameters of 36,837 crystal materials are obtained from the MP database [31] to establish the datasets including the energy per atom, formation energy, bulk modulus, and shear modulus. The CGCNN model is then trained, tested, and validated with a random dataset split of 60 : 20 : 20. The Adam optimization scheme [33] is adopted for the model parameter optimization with a learning rate of 0.01 and a batch size of 256. In this work, the dropout with p = 0.1 is applied to improve the accuracy based on the Monte Carlo operation, which is used as the Bayesian approximation tool to solve the uncertainty of the prediction results [34,35].

2. 2 Property prediction

The rapid generation of $Ti_3(Al_{1-x}A_x)C_2$ has been accomplished through a Python script that randomly occupies the Al-sites in Ti_3AlC_2 with A substitution atoms as shown in Fig. 2. Considering the changes of lattice parameters of the crystal structures resulted from A substitution at the Al-sites, a correction method that introduces the linear coefficient of the lattice constant at different composition x is adopted to reduce the error caused by the direct substitution. To predict the total energy per atom, 100 crystal structures of $Ti_3(Al_{1-x}A_x)C_2$ at different substitution concentrations are hence obtained and have been used as the inputs of the training models. Based on this, the crystal structure with the lowest total energy is screened out to determine the most stable one. Subsequently, the formation energy per atom, bulk modulus, and shear modulus are predicted to assess the stability and mechanical properties of $Ti_3(Al_{1-x}A_x)C_2$.

2. 3 Screening and verification

According to the two criteria of mixing energy and energy above hull calculated through the predicted total energy and formation energy per atom, the composition and configurations of $Ti_3(Al_{1-x}A_x)C_2$ with higher thermodynamic stability are screened out. Based on this, the elastic modulus of stable $Ti_3(Al_{1-x}A_x)C_2$ is predicted to screen the new MAX phase with tunable mechanical properties. Eventually, the DFT calculations with the Vienna *ab initio* simulation package (VASP) [36,37] and experimental measurements from literature are used to verify the prediction results. In our DFT calculations, the wave functions of the system are expanded by the plane-wave basis set [38]. The exchange-correlation potential between electrons is described by the Perdew, Becke, and Ernzerhof (PBE) functional of the Generalized Gradient Approximation (GGA) [39]. The Brillouin zone integrations are carried out by the Monkhorst-pack mesh [40]. For the Brillouin zone sampling, the *k*-point mesh parameters of 12 × 12 × 4 and 6 × 6 × 2 are set for the pure MAX phases and solid solution systems with a 2 × 2 × 2 supercell, respectively. Besides, the plane-wave cutoff energy of 700 eV, and the convergence criteria of 2×10^{-6} eV for electronic relaxation and 0.05 eV/Å for ionic force are used to ensure sufficient precision.

3 Results and discussion

3. 1 Evaluation of CGCNN model

In this section, the CGCNN model is evaluated to substantiate its feasibility and accuracy. The performances of the total energy and formation energy per atom predicted by the CGCNN model on 7367 test crystals are demonstrated in Figs. 3(a) and 3(b). It can be seen that, most of the predicted data points fall around the line $y = x$, indicating a high prediction accuracy of the CGCNN model. Among them, the goodness of fit (R^2) of the total energy and formation energy per atom yielded by the model are 0.9877 and 0.9883, respectively. Also, the mean absolute error (MAE) of them are 0.1317 and 0.0751 eV/atom, respectively, which are close to the accuracy of the DFT calculation with the MAE ranging from 0.081 to 0.136 eV/atom [41]. The performances of bulk modulus and shear modulus predicted through the CGCNN model on 1490 test crystals are shown in Figs. 3(c) and 3(d). The corresponding R^2 of the bulk modulus and shear modulus in the prediction results are 0.9554 and 0.9043, respectively. Also, the

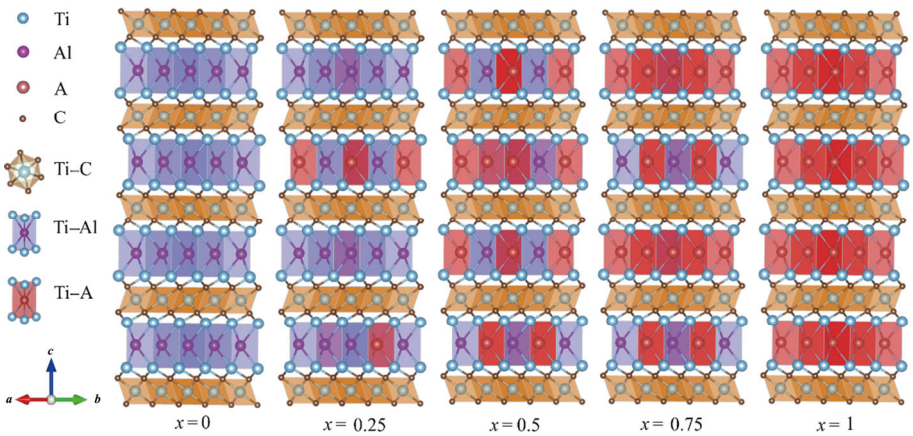

Fig. 2 Crystal structures of $Ti_3(Al_{1-x}A_x)C_2$ at different substitution concentrations.

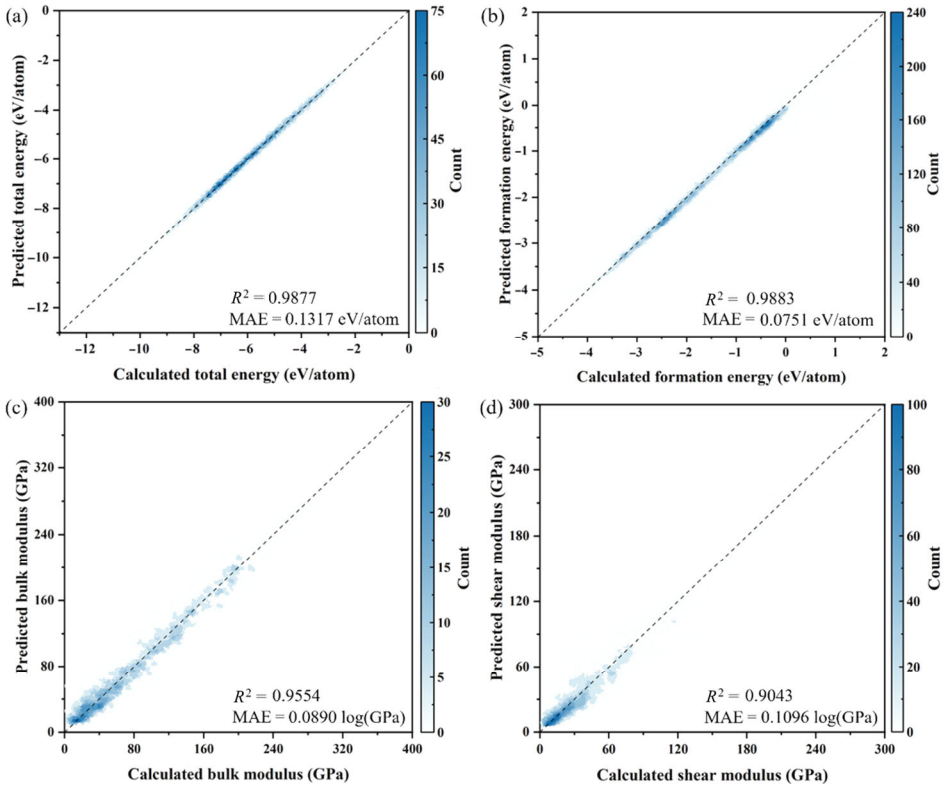

Fig. 3 2D histogram visualizing the predictive performance by CGCNN models: (a) total energy, (b) formation energy, (c) bulk modulus, and (d) shear modulus.

MAE are 0.0890 and 0.1096 log(GPa). Compared with the total energy and formation energy per atom, the prediction accuracy of the elastic modulus based on the CGCNN model is relatively lower, which is mainly ascribed to the smaller training dataset.

3. 2 Stability of $Ti_3(Al_{1-x}A_x)C_2$ predicted by CGCNN model

3.2.1 Screening criterion of mixing energy

To evaluate the stability of $Ti_3(Al_{1-x}A_x)C_2$, the mixing energy [42,43] is selected as a criterion, which can be calculated by Eq. (2):

$$E_{\text{mixing}} = E_{\text{Ti}_3(\text{Al}_{1-x}\text{A}_x)\text{C}_2} - (1-x)E_{\text{Ti}_3\text{AlC}_2} - xE_{\text{Ti}_3\text{AC}_2} \quad (2)$$

where $E_{\text{Ti}_3(\text{Al}_{1-x}\text{A}_x)\text{C}_2}$, $E_{\text{Ti}_3\text{AlC}_2}$, and $E_{\text{Ti}_3\text{AC}_2}$ are the total energy of $Ti_3(Al_{1-x}A_x)C_2$, Ti_3AlC_2, and Ti_3AC_2, respectively. These parameters can be predicted by the CGCNN model. Positive mixing energy indicates that there is a tendency to separate into the end-member pure MAX phases, which is unfavorable for the formation of the corresponding $Ti_3(Al_{1-x}A_x)C_2$ from the point of thermodynamics.

Figure 4 demonstrates the mixing energy of $Ti_3(Al_{1-x}A_x)C_2$ as a function of substitutional composition x. It can be found that, the mixing energy of all $Ti_3(Al_{1-x}A_x)C_2$ are in the range of [−200, 320] meV/atom, which are approximately consistent with the results calculated through the high throughput density functional clusters expansion by Arróyave *et al.* [42].

Herein, the mixing energy predicted by the CGCNN model based on the MP databases is calculated at 0 K. The $Ti_3(Al_{1-x}A_x)C_2$ solid solution are assumed to be thermodynamically stable within a buffer of about 50 meV/atom mixing energy. The reasons for the above choice are as follows. On one hand, room temperature (300 K) can account for 26 meV/atom of available thermal energy [24]. On the other hand, there is an average difference of around 24 meV/atom between the DFT and experimental measurements for the internal energy of elemental solids [44]. According to the calculated mixing energy, there are following two cases marked with different colors in Fig. 4.

As for the green region, the mixing energy of $Ti_3(Al_{1-x}A_x)C_2$ is less than 50 meV/atom. Studies have shown that Sn as the dopant in $Ti_3(Al_{1-x}Sn_x)C_2$ is helpful to stabilize solid solution [21,45]. According to the prediction, the substitutions of Pb, Sb, or Bi in

Ti_3AlC_2 are expected to obtain similar results, indicating that they can promote the formation of the corresponding solid solution. When A = Si, Ga, In, or Te, the mixing energy is close to 0, demonstrating that they are ideally mixed. In addition, these substitutions have almost negligible chemical interaction with Al, and thus they can be selected as probable candidates for the formation of $Ti_3(Al_{1-x}A_x)C_2$.

In view of the red region, the mixing energy of $Ti_3(Al_{1-x}A_x)C_2$ is greater than 50 meV/atom. These substitutions (S, Se, P, Au, Cd, Cu, Hg, Zn, or Tl) exhibit a larger endothermic interaction with Al in the A layer, resulting in a clear tendency of phase separation, which is not conducive to the formation of solid solution. Therefore, they are not appropriate choices for stabilizing substitutions in $Ti_3(Al_{1-x}A_x)C_2$ in this region.

The heat map in conjunction with the periodic table as shown in Fig. 5 depicts a more distinct exhibition of the mixing energy for all $Ti_3(Al_{1-x}A_x)C_2$. The bluer region indicates that the mixing energy is small, which is favorable for the formation of $Ti_3(Al_{1-x}A_x)C_2$ from the point of thermodynamics. On the contrary, the red region denotes that the mixing energy is large, indicating that the corresponding $Ti_3(Al_{1-x}A_x)C_2$ phases are unstable. Finally, ten candidate elements (A = Ga, Si, Sn, Ge, In, Pb, As, Bi, Te, or Sb) that make the mixing energy less than 50 meV/atom are selected for further screening.

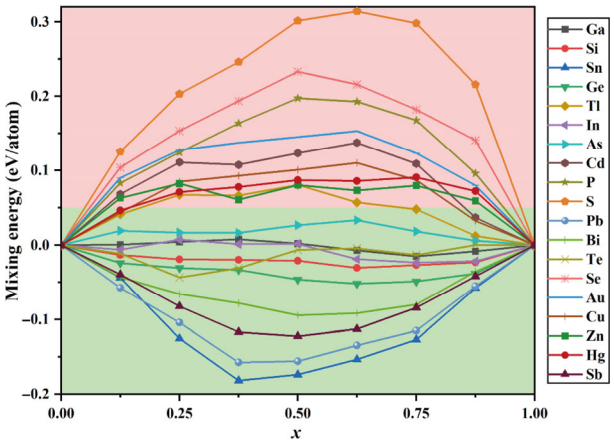

Fig. 4 Mixing energy of the $Ti_3(Al_{1-x}A_x)C_2$ with respect to composition x.

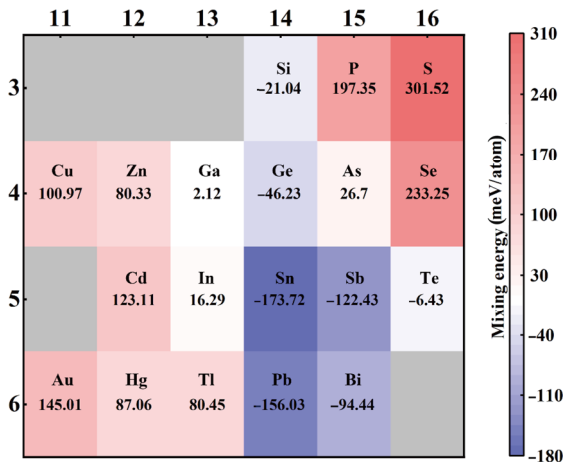

Fig. 5 Heat map of the mixing energy of $Ti_3(Al_{1-x}A_x)C_2$ at $x = 0.5$.

3.2.2 *Screening criterion of energy above hull*

For $Ti_3(Al_{1-x}A_x)C_2$ that passes the first screening by mixing energy, the energy above hull [24,46] is estimated by the grand-canonical linear programming (GCLP) method [47,48] to further measure their phase stability relative to competing ordered phases in the Ti–Al–A–C quaternary systems, which can be calculated through Eq. (3):

$$\Delta H_{stab} = \Delta H_f - E_{hull} \quad (3)$$

where ΔH_f is the formation energy of $Ti_3(Al_{1-x}A_x)C_2$ predicted by the CGCNN model, and E_{hull} is the convex hull energy relating to the ordered compounds that are retrieved from the Open Quantum Materials Database (OQMD). It is reported that the compound is generally stable or nearly stable with the energy above hull less than or equal to 50 meV/atom [24,45].

For the ten substitutions selected above, the energy above hull of $Ti_3(Al_{1-x}A_x)C_2$ is further calculated, and the results are shown in Fig. 6. Since the end-member MAX phases Ti_3AlC_2, Ti_3SiC_2, Ti_3GeC_2, and Ti_3SnC_2 are all known to be thermodynamically stable [49–51],

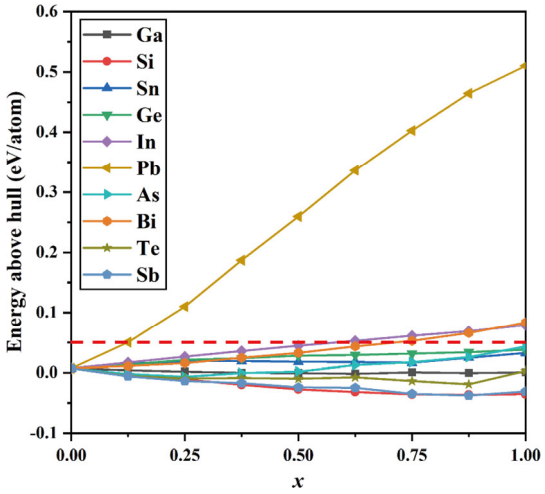

Fig. 6 Energy above hull of the $Ti_3(Al_{1-x}A_x)C_2$ with respect to composition x. The red dotted line indicates that the energy above hull is 50 meV/atom.

the energy above hull of them is zero according to the definition. Therefore, it can confirm the accuracy of calculated results. Figure 6 shows that for A = Ga, Si, Sn, Ge, As, Te, or Sb, the energy above hull of $Ti_3(Al_{1-x}A_x)C_2$ is less than 50 meV/atom regardless of x, suggesting that the formed solid solution is more stable. By contrast, for A = Pb, In, or Bi, the higher energy above hull indicates that the corresponding $Ti_3(Al_{1-x}A_x)C_2$ phases should not be stable from the point of thermodynamics.

In summary, according to the above two screening criteria, the seven elements (Ga, Si, Sn, Ge, Te, As, or Sb) are selected. The corresponding phases of $Ti_3(Al_{1-x}A_x)C_2$ are presumably easier to be synthesized through experiments from the point of thermodynamics, which lays a foundation for the follow-up prediction of the mechanical properties of $Ti_3(Al_{1-x}A_x)C_2$.

3. 3 Mechanical properties of $Ti_3(Al_{1-x}A_x)C_2$ predicted by CGCNN model

Herein, the optimized CGCNN model is used to predict the bulk modulus (B) and shear modulus (G) of $Ti_3(Al_{1-x}A_x)C_2$, and then the Young's modulus (E) and Poisson's ratio (ν) are obtained through Eq. (4) [52]:

$$E=\frac{9BG}{3B+G},\ \nu=\frac{3B-2G}{2(3B+G)} \tag{4}$$

where B, G, E, and ν of $Ti_3(Al_{1-x}A_x)C_2$ for different composition x are shown in Fig. 7. In general, B can be used to express the strength of average valence bond in crystal, G represents the shear deformation resistance caused by external pressure, E provides a measure of the stiffness and is inversely proportional to the critical thermal shock resistance, and ν reflects the shear stability and provides information regarding the properties of bonding force [53]. As shown in Fig. 7(a), when A = As, Si, Ge, Sn, or Sb, the B of $Ti_3(Al_{1-x}A_x)C_2$ increases with the increment of substitution concentration, indicating that these elements improve the average valence bond strength of the crystal and make the $Ti_3(Al_{1-x}A_x)C_2$ exhibit stronger resistance to deformation. For A = Ga or Te, the B varies little with the substitution concentration, but Te with a higher substitution concentration will reduce the B of $Ti_3(Al_{1-x}Te_x)C_2$. For G and E as shown in Figs. 7(b) and 7(c), the variation trends of different elements in different composition x

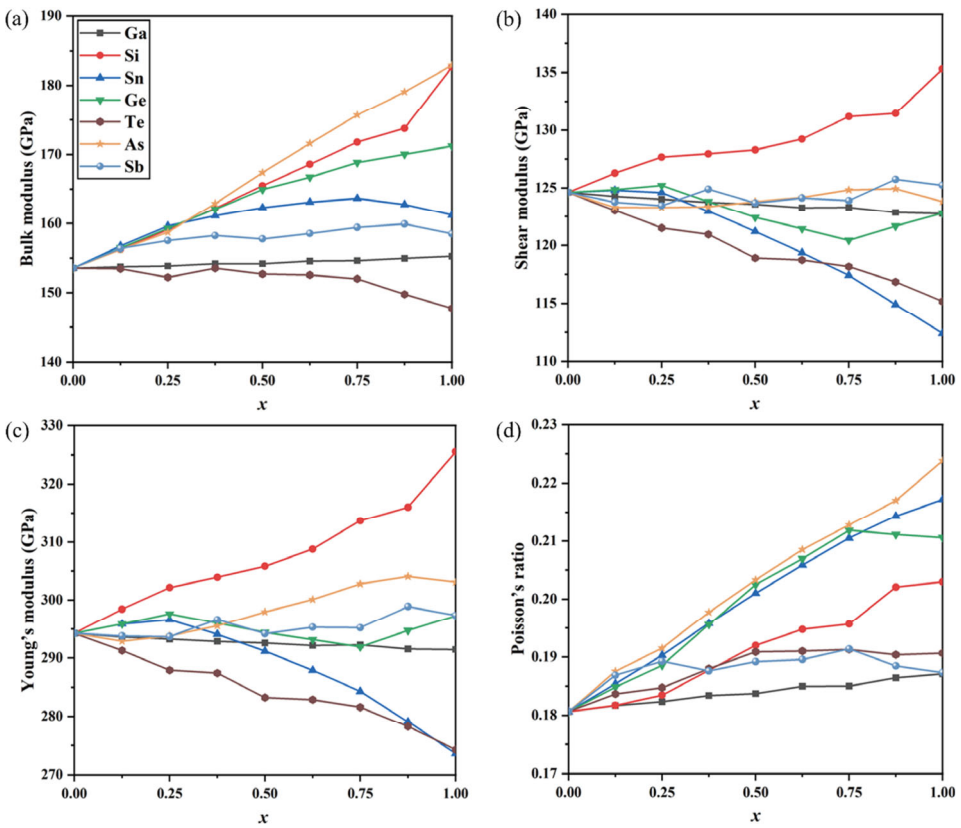

Fig. 7 Elastic properties of the $Ti_3(Al_{1-x}A_x)C_2$ with respect to substitution concentration x: (a) bulk modulus, (b) shear modulus, (c) Young's modulus, and (d) Poisson's ratio.

are almost accordant. When A = Si, the G and E increase as the Si concentration increases, indicating that $Ti_3(Al_{1-x}Si_x)C_2$ possesses stronger shear resistance and higher stiffness. For A = Ga, Ge, or Sb, there is a slight change in the G and E of $Ti_3(Al_{1-x}A_x)C_2$ with the variation of x. Similarly, the G of $Ti_3(Al_{1-x}As_x)C_2$ is slightly influenced by the substitution concentration of As, while the E is evidently increased. When substituted with Sn or Te, the E and G of $Ti_3(Al_{1-x}A_x)C_2$ decrease with the substitution concentration increasing, which indicates that Sn or Te can reduce the strength and thus endow Ti_3AlC_2 with better thermal shock resistance. For ν as seen from Fig. 7(d), the law is the same for all substitutions, i.e., ν for all of $Ti_3(Al_{1-x}A_x)C_2$ increases with the substitution concentration x increasing, which suggests that these substitutions contribute to the enhancement of plasticity.

According to the Pugh's criterion [54], the ratio of bulk modulus to shear modulus is used to predict whether the failure mode of $Ti_3(Al_{1-x}A_x)C_2$ is brittle or ductile, where $B/G = 1.75$ is the critical value to distinguish. It can be found from Fig. 8 that, the Pugh's module ratios of all systems are less than 1.75, indicating that the $Ti_3(Al_{1-x}A_x)C_2$ solid solution is brittle, which should originate from the ceramic properties. Whereas, with the increase of the substitution concentration, the Pugh's module ratio increases, i.e., the ductility of $Ti_3(Al_{1-x}A_x)C_2$ is improved, which is also in accordance with the trend of ν.

To further verify the accuracy of the CGCNN model, the values of E and G of $Ti_3(Al_{1-x}Si_x)C_2$ and $Ti_3(Al_{1-x}Sn_x)C_2$ at different composition x obtained via experimental measurements [20], the DFT calculations and the model predictions are compared as shown in Figs. 9(a) and 9(b). It can be seen that, the prediction results

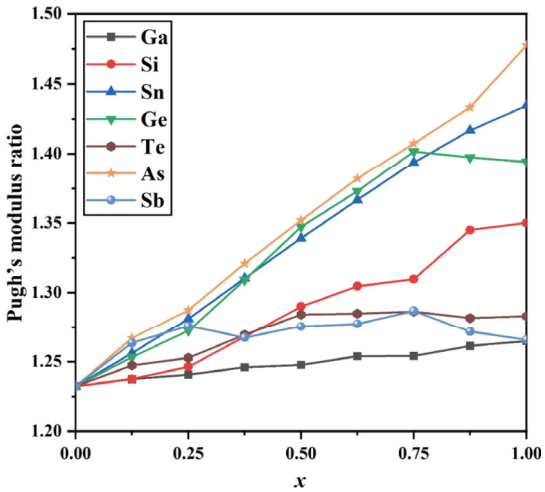

Fig. 8 Pugh's modulus ratio of the $Ti_3(Al_{1-x}A_x)C_2$ with respect to substitution concentration x.

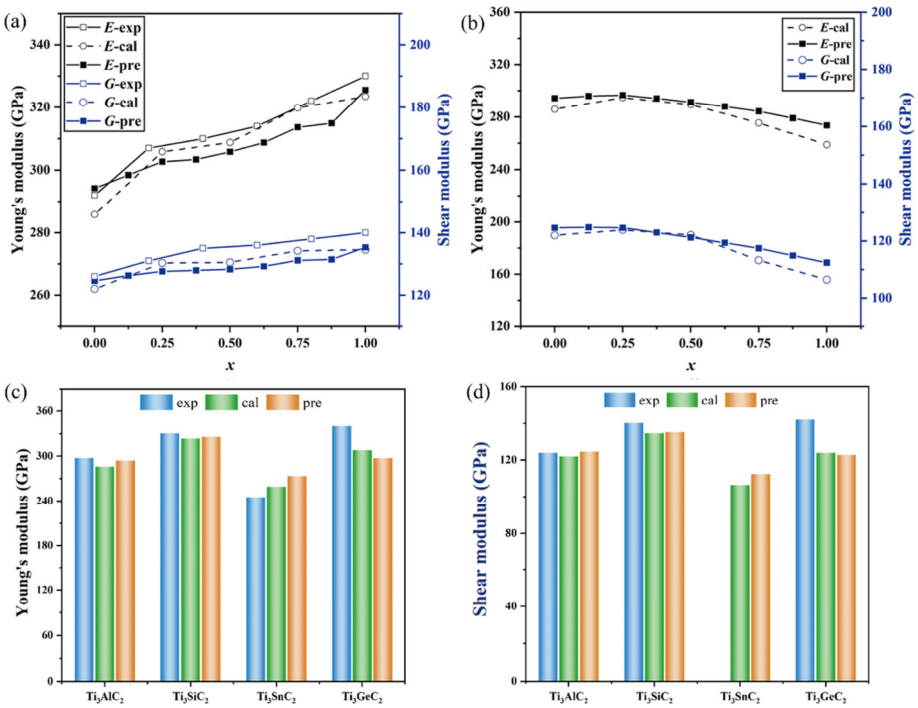

Fig. 9 Comparisons of experimental measurements (exp), DFT calculations (cal), and model predictions (pre): (a, b) the E and G of $Ti_3(Al_{1-x}Si_x)C_2$ and $Ti_3(Al_{1-x}Sn_x)C_2$, respectively, and (c, d) the E and G of Ti_3AlC_2, Ti_3SiC_2, Ti_3SnC_2, and Ti_3GeC_2, respectively. The experimental measurement of shear modulus of Ti_3SnC_2 is absent owing to the lack of the data in the literature.

of CGCNN model agree well with the DFT calculations and experimental measurements. In addition, the E and G of four pure MAX phases obtained by the experimental measurements [6,20], the DFT calculations, and the model predictions are also compared as shown in Figs. 9(c) and 9(d). The prediction results are well consistent with the values obtained experimentally and theoretically.

Furthermore, the bond parameters of $Ti_3(Al_{1-x}A_x)C_2$ (A = Si, Sn) as representatives are calculated via DFT to demonstrate the effect of A-site substitution on their mechanical properties. Figures 10(a) and 10(b) show the lengths of M–A, M_1–X, and M_2–X bonds of $Ti_3(Al_{1-x}A_x)C_2$ with respect to the substitution concentration x. Figures 10(c) and 10(d) correspond to the two-dimensional representations of the electron localization function (ELF) of $Ti_3(Al_{1-x}Si_x)C_2$ and $Ti_3(Al_{1-x}Sn_x)C_2$ on the (010) plane, respectively. As shown in Fig. 10, with the Si concentration increasing, the length of M–A bond decreases while the densities of electrons between M and A increase, indicating that the strength of M–A bond is enhanced. On the contrary, with the Sn concentration increasing, the increment in

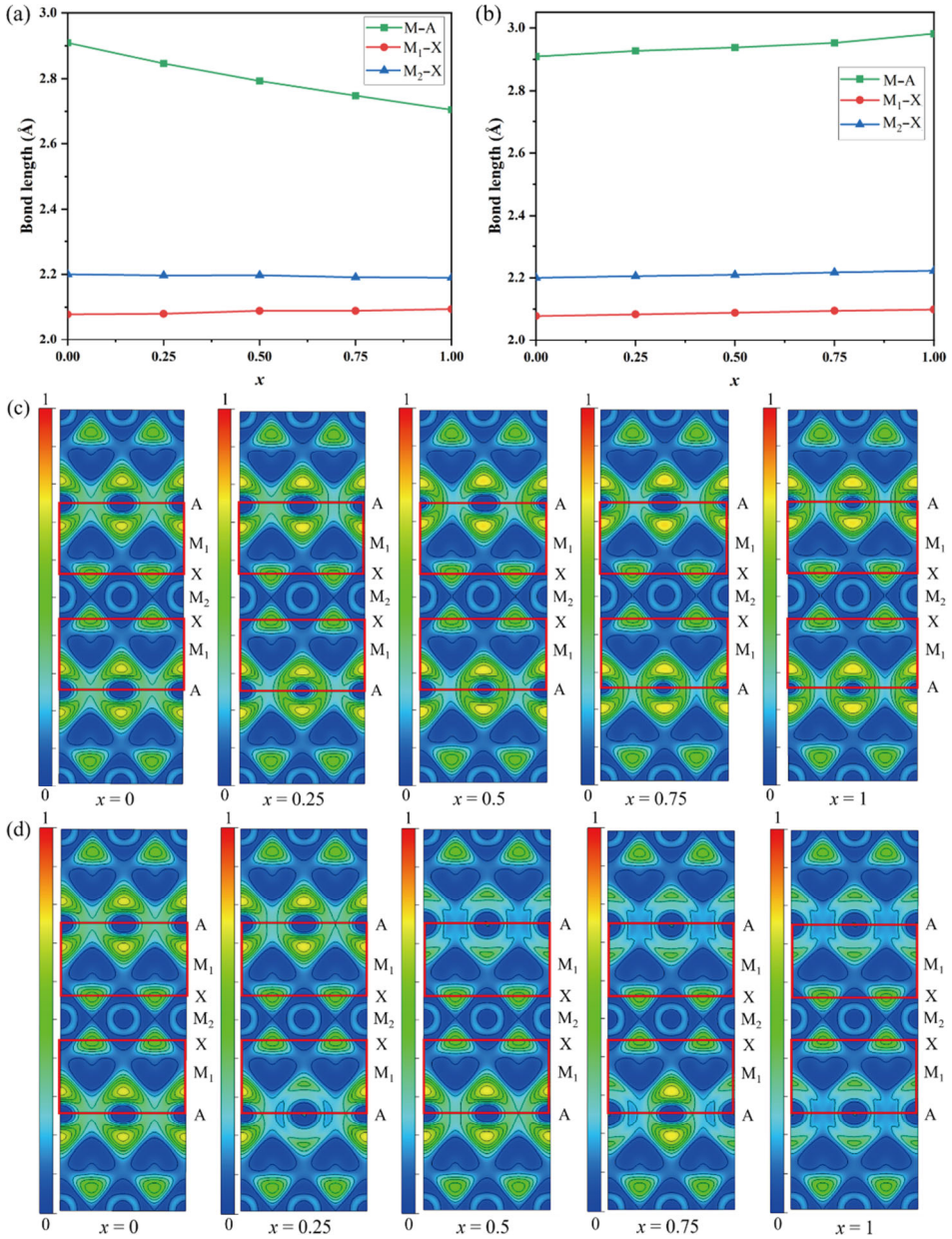

Fig. 10 (a, b) Lengths of M–A, M_1–X, and M_2–X bonds of $Ti_3(Al_{1-x}Si_x)C_2$ and $Ti_3(Al_{1-x}Sn_x)C_2$, respectively, where M_1 is the M element near the A element, and M_2 is the M element far from the A element. (c, d) Contour plots of the calculated ELF within the (010) plane of $Ti_3(Al_{1-x}Si_x)C_2$ and $Ti_3(Al_{1-x}Sn_x)C_2$ with respect to the substitution concentration x, respectively.

length of the M–A bond together with the decrement of electron densities between M and A suggest that the strength of M–A bond is weakened. These variations in bond strength are well consistent with the changes in mechanical properties of $Ti_3(Al_{1-x}A_x)C_2$ predicted, thereby verifying the feasibility and accuracy of CGCNN model.

4 Conclusions

To design new MAX phases with multifunctional applications, the optimized CGCNN model with a liner correction method has been proposed to elucidate the effect of A-site substitution on the upper and lower limits of mechanical properties of Ti_3AlC_2. The model can predict the mechanical properties of $Ti_3(Al_{1-x}A_x)C_2$ with great efficiency and the accuracy as per the DFT calculations. Among the selected nineteen elements, the $Ti_3(Al_{1-x}A_x)C_2$ phases are more stable when A = Ga, Si, Sn, Ge, Te, As, or Sb. With the increase of substitution concentration, Si or As improves the stiffness, while Sn or Te contributes to the thermal shock resistance of Ti_3AlC_2. Additionally, the plasticity of Ti_3AlC_2 can be greatly improved when As, Sn, or Ge is used as a substitution. This work can provide a reliable guideline for individual synthesis of high-performance MAX phases applied in various applications.

Acknowledgements

This work was supported by the National Science Fund for Distinguished Young Scholars (No. 52025041), the National Natural Science Foundation of China (Nos. 51904021, 51974021, and 52174294), and the National Key R&D Program of China (No. 2021YFB3700400).

Declaration of competing interest

The authors have no competing interests to declare that are relevant to the content of this article.

References

[1] Barsoum MW. The $M_{N+1}AX_N$ phases: A new class of solids: Thermodynamically stable nanolaminates. *Prog Solid State Chem* 2000, **28**: 201–281.

[2] Barsoum M, El-Raghy T. The MAX phases: Unique new carbide and nitride materials. *Amer Scientist* 2001, **89**: 334.

[3] Barsoum MW, Radovic M. Elastic and mechanical properties of the MAX phases. *Annu Rev Mater Res* 2011, **41**: 195–227.

[4] Radovic M, Barsoum MW. MAX phases: Bridging the gap between metals and ceramics. *Amer Ceram Soc Bull* 2013, **92**: 20–27.

[5] Zhou AG, Liu Y, Li SB, *et al*. From structural ceramics to 2D materials with multi-applications: A review on the development from MAX phases to MXenes. *J Adv Ceram* 2021, **10**: 1194–1242.

[6] Ching WY, Mo YX, Aryal S, *et al*. Intrinsic mechanical properties of 20 MAX-phase compounds. *J Am Ceram Soc* 2013, **96**: 2292–2297.

[7] Sokol M, Natu V, Kota S, *et al*. On the chemical diversity of the MAX phases. *Trends Chem* 2019, **1**: 210–223.

[8] Atikur Rahman M. Study on structural, electronic, optical and mechanical properties of MAX phase compounds and applications review article. *Am J Mod Phys* 2015, **4**: 75–91.

[9] Zuo CY, Zhong C. Screen the elastic and thermodynamic properties of MAX solid solution using DFT procedue: Case study on $(Ti_{1-x}V_x)_2AlC$. *Mater Chem Phys* 2020, **250**: 123059–123069.

[10] Zhao MX, Kou ZL, Zhang YJ, *et al*. Superhard transparent polycrystalline cubic boron nitride. *Appl Phys Lett* 2021, **118**: 151901–151905.

[11] Sahin FC, Kanbur HE, Apak B. Preparation of AlON ceramics via reactive spark plasma sintering. *J Eur Ceram Soc* 2012, **32**: 925–929.

[12] Gustafsson S, Falk LKL, Lidén E, *et al*. Pressureless sintered Al_2O_3–SiC nanocomposites. *Ceram Int* 2008, **34**: 1609–1615.

[13] Chen XZ, Luo LJ, Liu LY, *et al*. Microstructure and mechanical properties of hot-pressed Al_2O_3–mullite–ZrO_2–SiC composites. *Mater Sci Eng A* 2019, **740–741**: 390–397.

[14] Azzouz-Rached A, Rached H, Babu MH, *et al*. Prediction of double transition metal $(Cr_{1-x}Zr_x)_2AlC$ MAX phases as thermal barrier coatings: Insight from density functional theory. *Int J Quantum Chem* 2021, **121**: e26770.

[15] Hadi MA, Christopoulos SRG, Naqib SH, *et al*. Physical properties and defect processes of M_3SnC_2 (M = Ti, Zr, Hf) MAX phases: Effect of M-elements. *J Alloys Compd* 2018, **748**: 804–813.

[16] Cai LP, Huang ZY, Hu WQ, *et al*. Fabrication, mechanical properties, and tribological behaviors of Ti_2AlC and $Ti_2AlSn_{0.2}C$ solid solutions. *J Adv Ceram* 2017, **6**: 90–99.

[17] Cai LP, Huang ZY, Hu WQ, *et al*. Fabrication and microstructure of a new ternary solid solution of $Ti_3Al_{0.8}Si_{0.2}Sn_{0.2}C_2$ with high solid solution strengthening effect. *Ceram Int* 2018, **44**: 9593–9600.

[18] Fang Y, Liu XH, Feng YX, *et al*. Microstructure and mechanical properties of $Ti_3(Al,Ga)C_2/Al_2O_3$ composites prepared by *in situ* reactive hot pressing. *J Adv Ceram* 2020, **9**: 782–790.

[19] Niu YH, Fu S, Zhang KB, *et al*. Synthesis, microstructure,

and properties of high purity Mo_2TiAlC_2 ceramics fabricated by spark plasma sintering. *J Adv Ceram* 2020, **9**: 759–768.

[20] Gao HL, Benitez R, Son W, *et al*. Structural, physical and mechanical properties of $Ti_3(Al_{1-x}Si_x)C_2$ solid solution with x = 0–1. *Mater Sci Eng A* 2016, **676**: 197–208.

[21] Dubois S, Bei GP, Tromas C, *et al*. Synthesis, microstructure, and mechanical properties of $Ti_3Sn_{(1-x)}Al_xC_2$ MAX phase solid solutions. *Int J Appl Ceram Technol* 2010, **7**: 719–729.

[22] Curtarolo S, Setyawan W, Wang SD, *et al*. AFLOWLIB. ORG: A distributed materials properties repository from high-throughput *ab initio* calculations. *Comput Mater Sci* 2012, **58**: 227–235.

[23] Saal JE, Kirklin S, Aykol M, *et al*. Materials design and discovery with high-throughput density functional theory: The Open Quantum Materials Database (OQMD). *JOM* 2013, **65**: 1501–1509.

[24] Peterson GGC, Brgoch J. Materials discovery through machine learning formation energy. *J Phys: Energy* 2021, **3**: 022002–022014.

[25] Meredig B, Agrawal A, Kirklin S, *et al*. Combinatorial screening for new materials in unconstrained composition space with machine learning. *Phys Rev B* 2014, **89**: 094104.

[26] Ward L, Wolverton C. Atomistic calculations and materials informatics: A review. *Curr Opin Solid State Mater Sci* 2017, **21**: 167–176.

[27] Ramprasad R, Batra R, Pilania G, *et al*. Machine learning in materials informatics: Recent applications and prospects. *npj Comput Mater* 2017, **3**: 54.

[28] Li YQ, Liu LY, Chen WD, *et al*. Materials genome: Research progress, challenges and outlook. *Sci Sin Chimica* 2018, **48**: 243–255. (in Chinese)

[29] Butler KT, Davies DW, Cartwright H, *et al*. Machine learning for molecular and materials science. *Nature* 2018, **559**: 547–555.

[30] Xie T, Grossman JC. Crystal graph convolutional neural networks for an accurate and interpretable prediction of material properties. *Phys Rev Lett* 2018, **120**: 145301.

[31] Jain A, Ong SP, Hautier G, *et al*. Commentary: The Materials Project: A materials genome approach to accelerating materials innovation. *APL Mater* 2013, **1**: 011002.

[32] Noh J, Gu GH, Kim S, *et al*. Uncertainty-quantified hybrid machine learning/density functional theory high throughput screening method for crystals. *J Chem Inf Modeling* 2020, **60**: 1996–2003.

[33] Kingma D, Ba J. Adam: A method for stochastic optimization. In: Proceedings of the 3rd International Conference for Learning Representations, 2015.

[34] Gal Y, Ghahramani Z. Dropout as a Bayesian approximation: Representing model uncertainty in deep learning. In: Proceedings of the 33rd International Conference on Machine Learning, 2016.

[35] Srivastava N, Hinton G, Krizhevsky A, *et al.* Dropout: A simple way to prevent neural networks from overfitting. *J Mach Learn Res* 2014, **15**: 1929–1958.

[36] Kresse G, Furthmüller J. Efficiency of ab-initio total energy calculations for metals and semiconductors using a plane-wave basis set. *Comput Mater Sci* 1996, **6**: 15–50.

[37] Kresse G, Furthmüller J. Efficient iterative schemes for *ab initio* total-energy calculations using a plane-wave basis set. *Phys Rev B Condens Matter* 1996, **54**: 11169–11186.

[38] Kresse G, Joubert D. From ultrasoft pseudopotentials to the projector augmented-wave method. *Phys Rev B* 1999, **59**: 1758–1775.

[39] Perdew JP, Burke K, Ernzerhof M. Generalized gradient approximation made simple. *Phys Rev Lett* 1996, **77**: 3865–3868.

[40] Monkhorst HJ, Pack JD. Special points for Brillouin-zone integrations. *Phys Rev B* 1976, **13**: 5188–5192.

[41] Kirklin S, Saal JE, Meredig B, *et al*. The Open Quantum Materials Database (OQMD): Assessing the accuracy of DFT formation energies. *npj Comput Mater* 2015, **1**: 15010.

[42] Arróyave R, Talapatra A, Duong T, *et al*. Does aluminum play well with others? Intrinsic Al-A alloying behavior in 211/312 MAX phases. *Mater Res Lett* 2017, **5**: 170–178.

[43] Jiang C, Chroneos A. Ab initio modeling of MAX phase solid solutions using the special quasirandom structure approach. *Phys Chem Chem Phys* 2018, **20**: 1173–1180.

[44] Lejaeghere K, van Speybroeck V, van Oost G, *et al*. Error estimates for solid-state density-functional theory predictions: An overview by means of the ground-state elemental crystals. *Crit Rev Solid State Mater Sci* 2014, **39**: 1–24.

[45] Ai MX, Zhai HX, Zhou Y, *et al*. Synthesis of Ti_3AlC_2 powders using Sn as an additive. *J Am Ceram Soc* 2006, **89**: 1114–1117.

[46] Park CW, Wolverton C. Developing an improved crystal graph convolutional neural network framework for accelerated materials discovery. *Phys Rev Mater* 2020, **4**: 063801.

[47] Kirklin S, Meredig B, Wolverton C. High-throughput computational screening of new Li-ion battery anode materials. *Adv Energy Mater* 2013, **3**: 252–262.

[48] Akbarzadeh AR, Ozoliņš V, Wolverton C. First-principles determination of multicomponent hydride phase diagrams: Application to the Li–Mg–N–H system. *Adv Mater* 2007, **19**: 3233–3239.

[49] Nowotny VH. Strukturchemie einiger verbindungen der übergangsmetalle mit den elementen C, Si, Ge, Sn. *Prog Solid State Chem* 1971, **5**: 27–70.

[50] Pietzka MA, Schuster JC. Summary of constitutional data on the aluminum–carbon–titanium system. *J Phase Equilibria* 1994, **15**: 392–400.

[51] Dubois S, Cabioc'h T, Chartier P, *et al*. A new ternary nanolaminate carbide: Ti_3SnC_2. *J Am Ceram Soc* 2007, **90**: 2642–2644.

[52] Hill R. The elastic behaviour of a crystalline aggregate. *Proc Phys Soc A* 1952, **65**: 349–354.

[53] Hadi MA, Monira U, Chroneos A, *et al*. Phase stability and physical properties of $(Zr_{1-x}Nb_x)_2AlC$ MAX phases. *J Phys Chem Solids* 2019, **132**: 38–47.

[54] Pugh SF. XCII. Relations between the elastic moduli and

the plastic properties of polycrystalline pure metals. *Lond Edinb Dublin Philos Mag J Sci* 1954, **45**: 823–843.